Journal of Solid State Chemistry **165,** 65–73 (2002)
doi:10.1006/jssc.2001.9494, available online at http://www/idealibrary.com on IDEAL®

Strained Structure in $Ho_{0.5}Sr_{0.5}MnO_3$

C. Autret, C. Martin,[1] A. Maignan, M. Hervieu, and B. Raveau

Laboratoire CRISMAT, ISMRA et Université de Caen, CNRS UMR 6508, 6, boulevard Maréchal Juin, 14050 Caen, France

and

G. André and F. Bourée

LLB(CEA-CNRS), CEA/Saclay, 91191 Gif-sur-Yvette Cedex, France
E-mail: Christine.martin@ismra.fr

Received August 16, 2001; in revised form November 26, 2001; accepted December 21, 2001

The $Ho_{0.5}Sr_{0.5}MnO_3$ perovskite, synthesized in air, has been studied by combining neutron powder and electron diffraction techniques. The *Pnma*-type structure exhibits a strong tilting of the MnO_6 octahedra. This octahedra tilting and microtwinning involve a complex strained structure. No structural transition is observed down to 1.4 K, but short-range A-type antiferromagnetism running over only a few perovskite subcells is evidenced below $\approx$90 K. The different behavior of this perovskite compared to other $Ln_{0.5}Sr_{0.5}MnO_3$ perovskites is discussed in terms of *A*-site cationic mismatch. © 2002 Elsevier Science (USA)

Key Words: **manganites; electron microscopy; X-ray diffraction; neutron diffraction; magnetic properties, transport properties.**

INTRODUCTION

In the framework of the numerous studies on the colossal magnetoresistance (CMR) manganites, particular attention has been paid to the $Ln_{0.5}AE_{0.5}MnO_3$ oxides (*AE* is an alkaline earth), whose low-temperature antiferromagnetic behavior is closely related to the structure, and consequently depends on the nature of the *A* site cations (*A* = *Ln*, *AE*). It has indeed been shown that for perovskites involving small *A* cations such as the $Ln_{0.5}Ca_{0.5}MnO_3$ series (*Ln* = La, Pr, Nd, Sm), a structural transition from a *Pnma*-type structure to a charge ordered structure, built up from alternating Mn^{3+} and Mn^{4+} stripes, is obtained at decreasing temperature (1–9). Such a charge ordering is very stable, leading to a CE-type antiferromagnetic (AFM) state, which hinders the appearance of CMR, at least for smaller cations. In contrast, for larger cations, no charge ordering is observed as shown for instance for $Pr_{0.5}Sr_{0.5}MnO_3$, which exhibits a transition from an I to an F-type structure associated with an A-type AFM state at low temperature (10, 11), and CMR is observed (12). Nevertheless in the $Ln_{0.5}Sr_{0.5}MnO_3$ series the structural evolution is more complex, involving the appearance of charge ordering and CE-type antiferromagnetism at low temperature for *Ln* = Nd (13) closely associated with an *Imma* structure at room temperature as shown by Woodward *et al.* (14). Similarly, the appearance of CMR in $Gd_{0.5}Sr_{0.5}MnO_3$ has been attributed to the collapse of the charge ordered state, which coexists below 42 K with a cluster glass state (15, 16).

In order to understand the particular magnetic and transport properties of the $Ln_{0.5}Sr_{0.5}MnO_3$ series with small Ln^{3+} cations (Gd to Ho) a detailed structural study is absolutely necessary. In an attempt to obtain the holmium compound working in air as previous authors have done, we have synthesized the $Ho_{0.5}Sr_{0.5}MnO_3$ perovskite, whose structure has been studied by electron microscopy and X-ray and neutron diffraction. We show that whatever the temperature, ranging from 1.4 K to 300 K, this oxide exhibits a strained structure, whereas at low temperature below 90 K, a short-range antiferromagnetism, probably from A type, is observed.

EXPERIMENTAL

The sample was prepared by solid state reaction at high temperature of stoichiometric mixtures of Ho_2O_3, $SrCO_3$, and MnO_2, intimately ground in an agate mortar. The mixture was first heated in air at 1000 °C, sintered at 1200 °C, then at 1500 °C for 12, slowly cooled down to 800 °C, and then quenched to room temperature.

The X-ray powder diffraction (XRPD) analyses were carried out at room temperature with a Philips

[1]To whom correspondence should be addressed. Fax: 33 2 31 95 16 00.

0022-4596/02 $35.00

diffractometer working with Cu$K\alpha$ radiations (λ_1 = 1.5406 Å and λ_2 = 1.5443 Å) in the range $10° \leq 2\theta \leq 110°$ by increment of 0.02° in 2θ.

Neutron experiments were carried out at the LLB (France) on the G41 diffractometer ($\lambda = 2.4266$ Å, $17° < 2\theta < 97°$). The sample was first cooled down to liquid helium temperature and patterns were recorded by increasing the temperature. High-resolution data were also registered at 300 K on the 3T2 diffractometer ($\lambda = 1.2251$ Å, $6° < 2\theta < 125°$). Crystalline and magnetic structures were analyzed with the Rietveld method using the Fullprof program.

Samples for electron microscopy (EM) study were prepared by smoothly crushing the crystallites in alcohol. The small flakes were deposited on a holey carbon film, supported by a copper grid. The electron diffraction (ED) study was carried out at room temperature with a JEOL 200CX electron microscope. The ED study versus temperature and the bright/dark field imaging were made with a JEOL 2010 electron microscope fitted with a double tilt cooling sample holder (N_2 liq). The high resolution electron microscopy (HREM) study was made with a TOPCON 002B electron microscope operating at 200 kV (Cs = 0.4 mm). The three transmission electron microscopes are equipped with energy dispersive spectroscopy (EDS) analyzers.

The resistivity measurements were performed from room temperature down to 5 K (in 0 and 7 T) by the four-probe method. The *T*-dependent magnetization data were recorded by warming, with a vibrating sample magnetometer, in 1.4 T after a zero-field-cooled process, and both field-dependent magnetization and *T*-dependent ac-susceptibility curves were registered by using an ac–dc SQUID magnetometer.

RESULTS AND DISCUSSION

Following the above experimental conditions a single-phased material is synthesized, as shown further from X-ray, neutron diffraction, and electron microscopy investigations. The EDS analysis carried out on many microcrystals shows that the cationic distribution is homogeneous and corresponds to the nominal one "$Ho_{0.5}Sr_{0.5}Mn$." Of 100 analyzed crystals, only one was found to be an impurity, from H_2O_3 type.

The structural study was carried out, using concomitantly XRPD, neutron powder diffraction (NPD), and electron microscopy, but to clarify, electron microscopy is presented separately.

Room Temperature Electron Microscopy

The reflections are sharp and the electron diffraction investigation shows the good crystallinity of the sample. Tilting around the crystallographic axes makes it possible to reconstruct the reciprocal space for numerous grains. The electron diffraction patterns of all these crystallites are characteristic of a *Pnma*-type structure, with $a \approx a_p \sqrt{2}$, $b \approx 2a_p$, and $c \approx a_p \sqrt{2}$ (a_p being the parameter of the cubic perovskite cell). They also show that twinning phenomena systematically take place in the grains. This effect is commonly observed in the manganites as a result of the orthorhombic distortion of the perovskite. The tilting of the octahedra arises along the $\{100\}_p$ equivalent directions of the perovskite subcell, i.e., the [010], [−101], and [101], directions of the orthorhombic cell. This is illustrated in the ED patterns given in Fig. 1. The [010] and [101] zones are superimposed (the corresponding indexation is given in Fig. 1b).

The bright field and high-resolution images of the crystallites exhibit a particular contrast, which consists of a cobbled arrangement of dark and less dark areas. One example is given in Fig. 2. This is the signature of a strain effect. The enlarged HREM images make it possible to understand the origin of this phenomenon. They clearly evidence a "patchwork" of twinning domains. The example displayed in Fig. 3a, which corresponds to the ED pattern in Fig. 1a, shows that [010] and [101] domains coexist and, moreover, each of them exhibits two possible 90° orientations. The spectacular character of this sample is the size of the domains. The average size of the domains is a few tens of nanometers but, locally, the size can be lowered to a few nanometers, as shown in Fig. 3b.

The second step of this study was to determine, if possible, the crystallographic nature of the domains that make up the patchwork. The electron diffraction patterns actually exhibit the peaks expected for a *Pnma* structure. Nevertheless, due to the complexity of the microstructure, they do not make it possible to exclude definitely the presence of a secondary perovskite phase, which would have different extinction conditions. Typically, one must check the eventual presence of *Imma*-type domains, as observed in the $Ln_{0.5}Sr_{0.5}MnO_3$ phases with *Ln* = Nd and Sm where the two structures, namely *Pnma* and *Imma*, are observed (14), or distorted monoclinic $P2_1/m$ or $P2_1/c$ domains, as observed in $Pr_{0.7}Ca_{0.25}Sr_{0.05}MnO_3$ (17). This exploration was carried out with the help of the experimental images we obtained in our previous studies on manganites and the theoretical images calculated with three sets of positional parameters corresponding to the *Pnma* (this work), the *Imma*, and the $P2_1/c$ structures (17).

The simulated images were calculated by varying the focus values from 0 to −130 nm, in step of 5 nm, and the crystal thickness from 1.5 to 12 nm. Considering all these through focus series, it clearly appears that the images exhibit significant differences only for specific focus values. The more the structure is distorted, the more the contrast difference is indeed important.

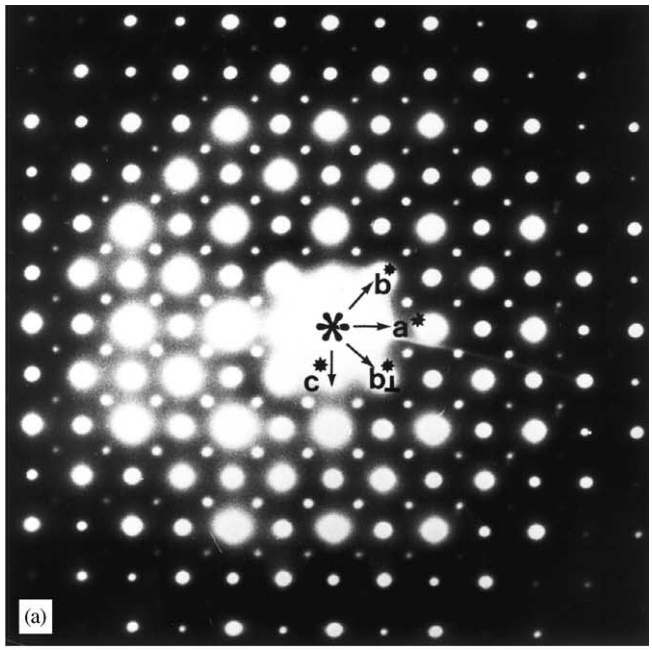

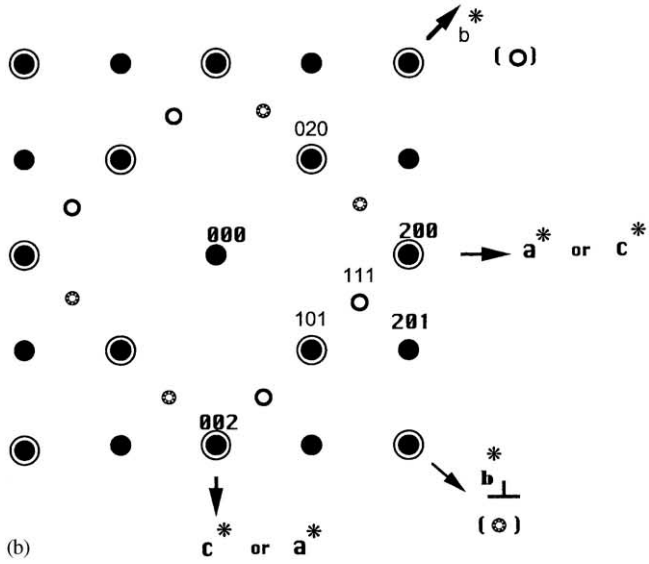

FIG. 1. (a) ED pattern showing superimposed [010] and [101] zones, and, (b) indexation of the pattern (b and $b_\perp$ refer to [101] variants with perpendicular [010]* directions).

All the images were recorded in numerous areas where the [010] domains exhibit contrasts in favor of the *Pnma* structure. The most characteristic images are obtained for focus values where the brighter dots are correlated to the low electron density zones, i.e., associated with the oxygen positions. An example of an enlarged [010] image illustrating this point is shown in Fig. 4. The rows of bright dots, spaced 2.7 Å along $\vec{a}$ and $\vec{c}$ (corresponding to the equivalent $[110]_p$ directions of the perovskite unit cell), are waving in

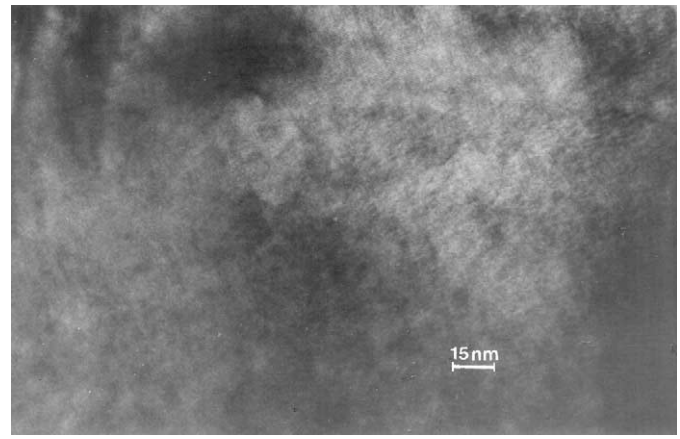

FIG. 2. Overall image showing the strained structure of the compound.

agreement with the simulated images of the *Pnma*-type structure. The enlarged theoretical image is calculated for a focus value close to −750 Å, a crystal thickness of 45 Å, and the positional parameters of Table 1; such a waving of the rows of dots is not compatible with the *Imma*-type images.

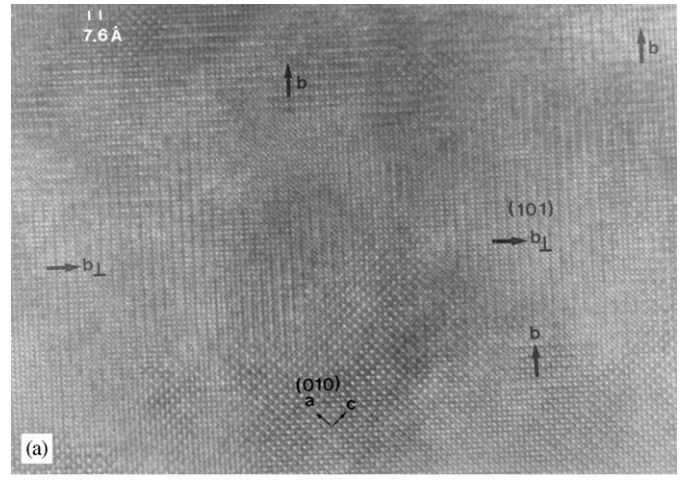

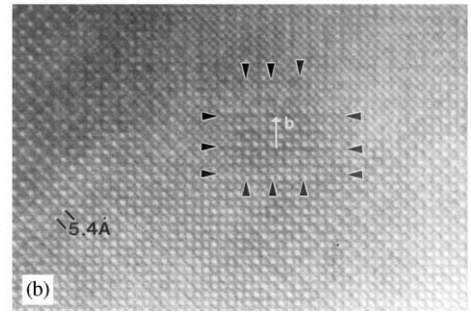

FIG. 3. (a) High-resolution image corresponding to [010] and [101] zones, illustrating the patchwork-like arrangement of the domains. (b) Image of a few-nanometers-wide domain.

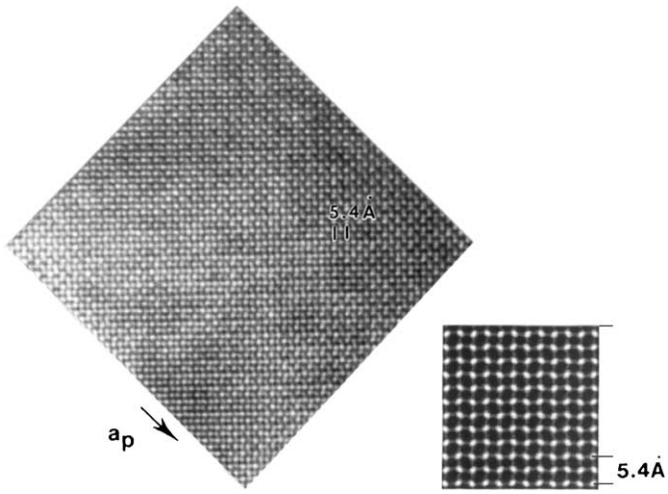

FIG. 4. Enlarged [010] high-resolution image, recorded for a focus value close to −750Å, showing the waving of the bright dots, compatible with a *P*-type structure. The calculated image corresponds to a crystal thickness of 45 Å.

Moreover, looking at the images for grazing incidence (along the black arrows) shows irregular waving of the rows of bright dots, which suggests different types of very local distortions.

Along [101], the experimental though focus series confirm that in many zones the contrast is characteristic of the *Pnma* structure, even though there exist numerous zones where the contrast fits neither the *Pnma* nor the *Imma* structure. One example is given in Fig. 5, where the alternation of two types of rows along **b** is more pronounced in some areas and less in others (bottom part of the image). Such an effect was previously observed in $Pr_{0.7}Ca_{0.25}Sr_{0.05}MnO_3$ (17) and could be simulated by a local lowering of the symmetry to monoclinic $P2_1/c$, allowing the oxygen atoms at the level of the Mn positions to be displaced separately in two adjacent perovskite layers.

From these images, one can therefore conclude about the lowering of the symmetry with regards to the classical *Pnma*-type symmetry. However, the empirical waving effect of the rows (see, for instance, Fig. 5 at the grazing incidence along [010]), viewed along different directions, suggests that the positions of the oxygen atoms could be variable, and consequently, their positions could be hardly accurately refined using any single space group. Note that the strain effect between the different domains is locally relaxed through dislocation mechanisms, as shown in Fig. 6.

Thus, this HREM study shows that the structure of $Ho_{0.5}Sr_{0.5}MnO_3$ is highly strained and could be described as derived from the orthorhombic *Pnma* structure with a small and not regular deviation of the oxygen position in the MnO_2 layer. Another characteristic concerns the exceptionally small size of the twinning domains and the absence of coherency of the twinning boundaries.

TABLE 1
$Ho_{0.5}Sr_{0.5}MnO_3$: Room Temperature Crystallographic Data (from 3T2 Data)

SG = *Pnma*

a = 5.4142(2) Å
b = 7.6221(3) Å
c = 5.3945(2) Å
V = 222.6 Å^3

	Site	x	y	z	B (Å^2)
Ho, Sr	4c	0.0311(4)	0.25	−0.0061(9)	0.67(3)
Mn	4b	0	0	0.5	0.52(4)
O_1	4c	−0.0101(8)	0.25	0.4335(8)	1.68(7)
O_2	8d	0.7177(6)	−0.0308(3)	0.2824(7)	1.47(5)

R_p = 3.72
χ^2 = 3.31
R_f = 4.08

⟨Interatomic distances (in Å) — and multiplicity — and angles⟩ (°)

Mn–O_1	1.940(1) × 2
Mn–O_2	1.940(3) × 2
Mn–O_2	1.941(3) × 2
Mn–O_1–Mn	158.4(1)
Mn–O_2–Mn	159.8(2)

X-Ray and Neutron Diffraction at Room Temperature

The X-ray and medium resolution neutron diffraction patterns, recorded at room temperature, are given

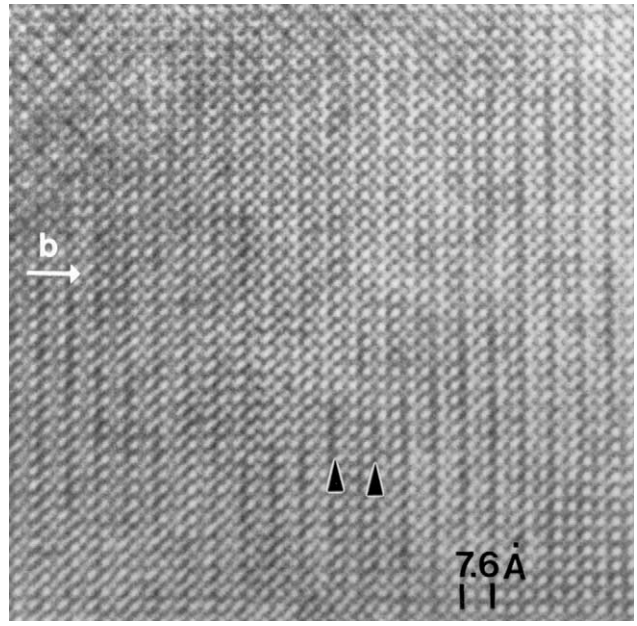

FIG. 5. Example of waving contrast in the [101] images.

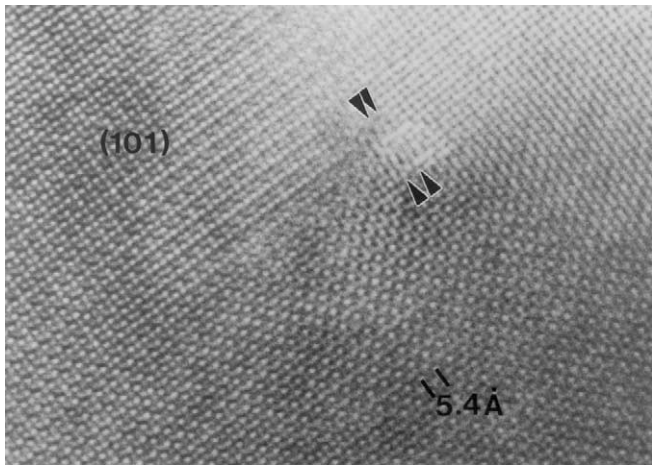

FIG. 6. Example of dislocation mechanism.

in Figs. 7a and 7b. All the reflections are indexed in the *Pnma* space group. Nevertheless some of the peaks exhibit an anomalous width. As previously reported for $Y_{0.5}Sr_{0.5}MnO_3$ by Woodward *et al.* (14), the sharp peaks are those which obey the reflection conditions of an *Imma*-type structure and the broadened ones those which violate the *Imma* conditions. Note that due to the same cationic size for Ho and Y, the *A*-site cationic average size is the same for $Ho_{0.5}Sr_{0.5}MnO_3$ and $Y_{0.5}Sr_{0.5}MnO_3$ ($\langle r_A \rangle 1.191$ Å). The size difference between Sr and Ho or Y involves a large *A*-site cationic size mismatch quantified by the variance $\sigma^2 = 1.4 \times 10^{-2}$ Å^2 (18). This broadening effect of certain reflections was attributed to a decrease of the coherence length of the in-plane tilt about **b** (14). Analysis of high-resolution NPD data is reported in Table 1, with the main calculated interatomic distances and angles. The observed and refined patterns are shown in Fig. 7c. Let us note that the calculations were made with two *hkl* files, corresponding to the odd and even "$h+k+l$,", that is to the broad and thin peaks, respectively (upper and lower Bragg sticks in Fig. 7). In fact, using this two-*hkl*-files option for the refinement improves significantly the fit and allows the determination of two coherence lengths. Due to the small intensities of the broad peaks, the neutron diffraction G41 (high-flux-diffractometer) data were used to estimated these coherence lengths to 120 and 2500 Å, for the *Pnma* and *Imma* lines, respectively.

This study shows the pseudo-cubic character of the perovskite subcell ($b/\sqrt{2} = 5.389$ Å) < ($c = 5.394$ Å) < ($a = 5.414$ Å)] and evidences an O′-type structure, with a weak orthorhombic distortion (only $\approx 0.12\%$), characteristic of a large cooperative buckling determined by the steric effect (19). The small difference between the cell parameters may contribute to the appearance of the exceptional micro-twinning evidenced by ED. However, the remarkable feature deals with the fact that the MnO_6 octahedra tilting is very strong, involving Mn–O–Mn

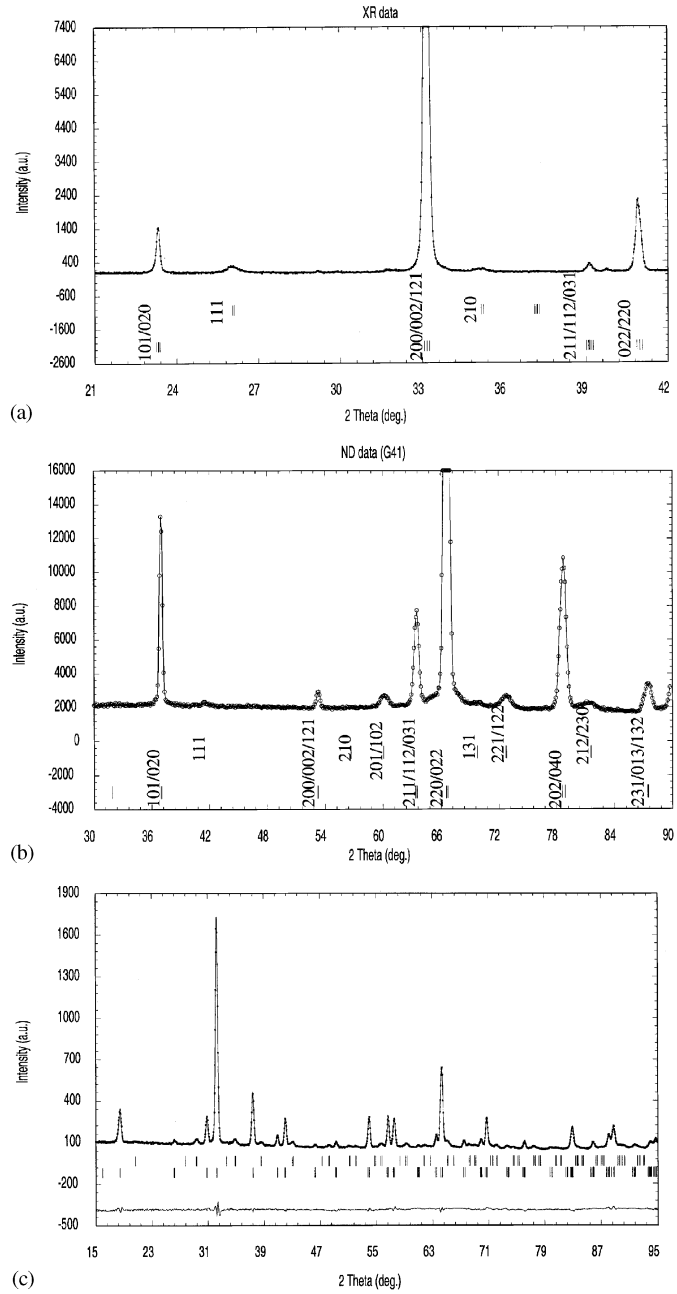

FIG. 7. Diffraction patterns at room temperature ((a) X-ray and (b) medium-resolution neutron) showing the broadening of the peaks, differentiating the *Pnma* and *Imma* space groups. (c) Observed, calculated, and difference NPD (high-resolution) patterns.

angles of $\approx 158°$ and $\approx 160°$, the MnO_6 octahedra being described by very close Mn–O distances:2 d(Mn–O_{ap}) = 2 d(Mn–O_{eq}) ≈ 1.940 Å and 2 d(Mn–O_{eq}) ≈ 1.941 Å. Thus, the structure exhibits regular MnO_6 octahedra but is distorted ($a^-b^+a^-$ tilt system in the Glazer notation (20)) with large deviations from 180° in the Mn–O–Mn angles.

The refinement of the occupancy factors for the two oxygen positions leads to a tiny oxygen deficiency leading

to an oxygen content of 2.99(1) per perovskite unit, in agreement with the chemical titration. Nevertheless, the oxygen *B* factors remain high (see Table 1) for both oxygen sites. The Fourier difference maps did not evidence phenomena that could explain these high values; consequently, the attempts to split the oxygen sites or to refine the anisotropic Debye–Waller factors do not improve the fit. Let us note that these rather high thermal parameters could be correlated to the odd peaks' broadening, which may be due to small displacements of the oxygens from their theoretical sites, as shown by electron microscopy. However, refinement of the high-resolution NPD pattern in the $P2_1/c$ space group was unsuccessful, even constrained this calculation did not reach the convergence. In fact, as shown from the HREM images, the oxygens are displaced from their ideal positions in the *Pnma* space group, so that a better description should be obtained with the $P2_1/c$ space group. However the atomic displacements are tiny and chaotic and, by the way, cannot be refined in a single monoclinic space group.

These distortions of the oxygen framework seem necessary to stabilize such a structure with a large *A*-site cationic mismatch and a small *A*-site average radius. In fact, in the $Ln_{0.5}Sr_{0.5}MnO_3$ series, under our synthesis conditions, the formation of the compounds becomes difficult for the smaller *Ln* cations. For instance, Er- or Tm-based samples are biphasic, as the hexagonal $ErMnO_3$ or $TmMnO_3$ phase appears as an impurity in the perovskite (21). It is well known that for small $\langle r_A \rangle$ a large range of σ^2 is possible but that inhomogeneities appear when disorder is introduced, destabilizing the perovskite structure (22). Consequently, a strained structure is evidenced for the $Ho_{0.5}Sr_{0.5}MnO_3$ manganite. Moreover, all attempts to decrease the strain in this compound (by annealing in oxygen flow at low temperature or at high temperature with slow cooling till room temperature) were unsuccessful.

Evolution of the Structure versus Temperature

The electron diffraction patterns registered down to 92 K do not show any structural transition; in particular no extra reflections characteristic of charge ordering are observed in contrast to $Ln_{0.5}Ca_{0.5}MnO_3$ perovskites (1–9) and to $Nd_{0.5}Sr_{0.5}MnO_3$ (13). Two basal ED patterns of the $Ho_{0.5}Sr_{0.5}MnO_3$ sample, recorded at 92 K, are given in Fig. 8. Both are the superposition of at least two variants, due to the aforementioned twinning phenomena. [100] and [001] ED patterns are superposed in Fig.8a, [010] and two variants of the [101] patterns in Fig. 8b. One observes that all the reflections are cross-shaped (see the high-order reflections in Figs. 8a and 8b); this suggests an evolution of one parameter, inducing an increase of the strain

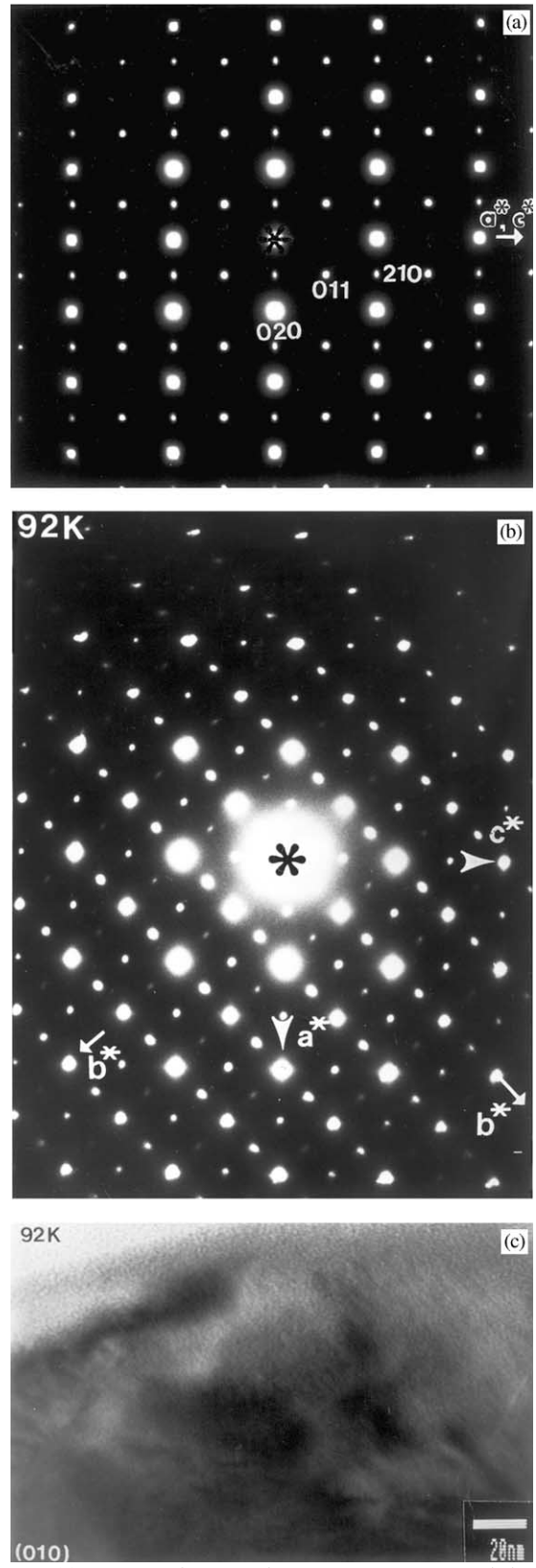

FIG. 8. (a) Superposed [100] and [001] ED patterns recorded at 92 K. (b) Superposed [101] and [010] ED patterns recorded at 92 K. (c) Bright field image recorded at 92 K.

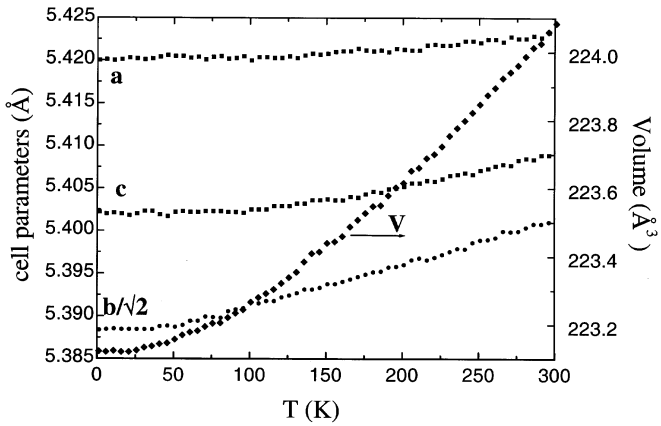

FIG. 9. Temperature dependence of the cell parameters (from G41 data).

effect, with regards to room temperature. This is clearly observed in the bright field images recorded at 92 K, as shown in Fig. 8c.

The medium-resolution NPD patterns registered between 300 and 1.4 K (Fig. 9) show the structure remains from *Pnma* type: the *a* and *c* parameters decrease slightly as *T* decreases (*a* is nearly constant), whereas the decrease of *b* is more pronounced. This temperature dependence is in agreement with the EM observations showing an increase of the strain, at low temperature, associated with a larger variation for one lattice parameter. Below $\approx$ 90 K, a very broad and small peak develops smoothly at small angles (Fig. 10), which can be assigned to A-type antiferromagnetism, as in $Pr_{0.5}Sr_{0.5}MnO_3$ (11). The refinement of this AFM structure, that is ferromagnetic planes antiferromagnetically coupled (8, 9), leads to a magnetic moment of $\approx 1\,\mu_B$ at 1.4 K, but the coherence length close to 45 Å shows that this phenomenon corresponds to short-range antiferromagnetism, running over less than 10 perovskite subcells only.

Magnetic and Transport Properties

In contrast to $Gd_{0.5}Sr_{0.5}MnO_3$, which exhibits CMR properties connected to irreversibility in the magnetization, the present $Ho_{0.5}Sr_{0.5}MnO_3$ manganite does not show CMR properties but a negative magnetoresistance of only -60% in a 7-T magnetic field as shown in Fig. 11 (right *y* axis). In fact, both 0- and 7-T curves exhibit a semiconducting-like behavior, consistent with a lack of field-induced ferromagnetism (no irreversiblity in the *M*(H) curves of Fig.12). This behavior contrasts with the field-induced ferromagnetism responsible for the resistivity drop

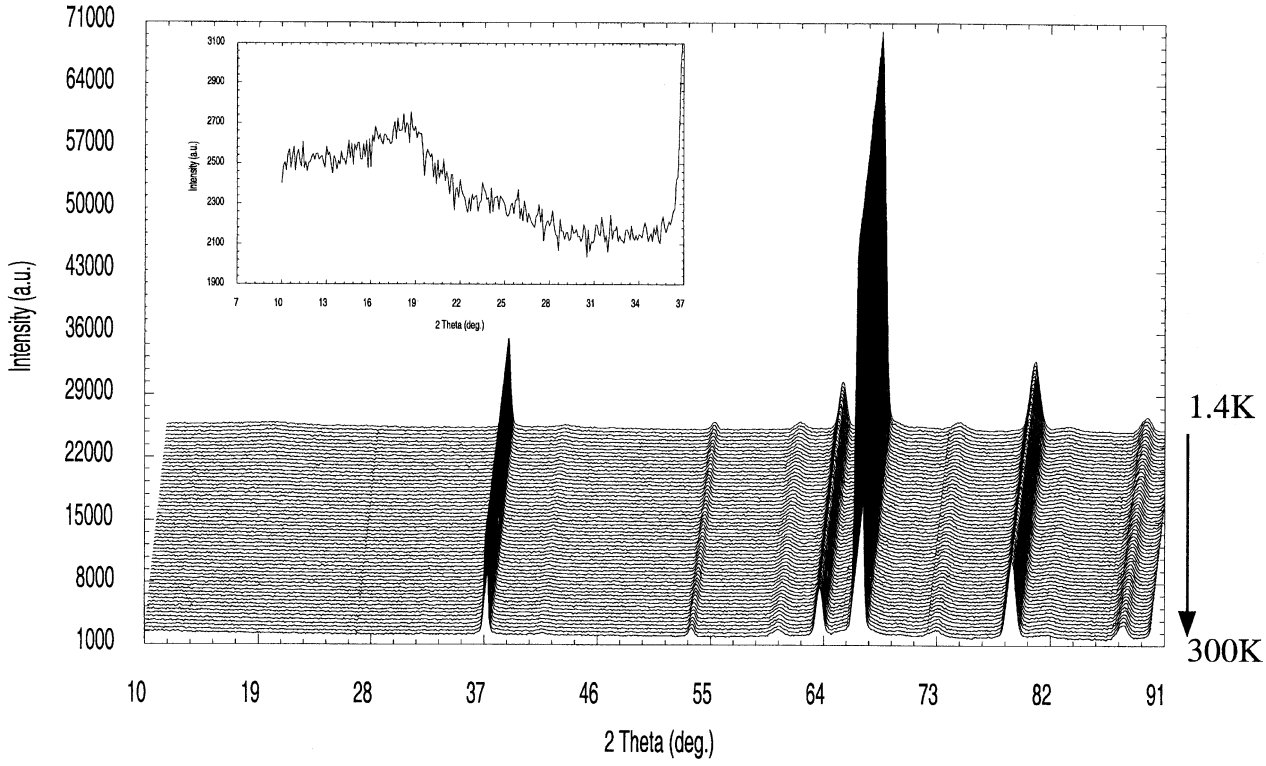

FIG. 10. Evolution of the ND patterns versus *T*. Inset: enlargement of the small angles zone.

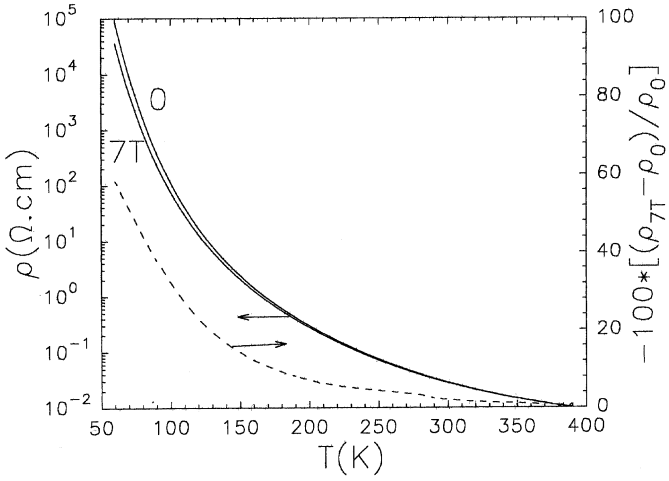

FIG. 11. T dependence of the resistivity ρ for a bar of $Ho_{0.5}Sr_{0.5}MnO_3$ registered upon cooling from 400 K at 0 and then at 7 T. The magnetoresistance percentage is also given (right y-axis).

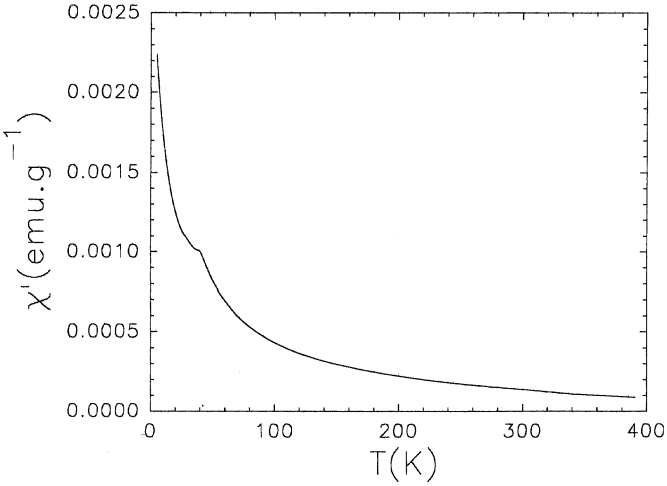

FIG 13. Ac $\chi'(T)$ curve of $Ho_{0.5}Sr_{0.5}MnO_3$ collected within $h_{ac} = 3$ Oe with frequency $f = 666$ Hz.

in $Gd_{0.5}Sr_{0.5}MnO_3$. For the latter, the presence of ferromagnetic clusters was shown from ac-susceptibility measurements as a function of T exhibiting a cusp characteristic of the freezing of the clusters (15). The ac $\chi(T)$ curves of $Ho_{0.5}Sr_{0.5}MnO_3$ do not exhibit a cusp but only a slight change of slope at 40 K (Fig. 13). This is consistent with much less numerous clusters in the Ho-based manganite. Most probably, the strained structure induced by the large A-site cationic size mismatch hinders the Mn–O–Mn ferromagnetic coupling. As a consequence magnetic field values larger than 7 T are necessary to overcome the critical field value of this compound.

CONCLUDING REMARKS

The average size of the A-site cations and of the corresponding A-site mismatch, characterizing the size difference between Ln^{3+} and Sr^{2+} (18, 22), are thus two relevant factors in the $Ln_{0.5}A_{0.5}MnO_3$ system. It is thus of interest to compare the Ho-based manganite with the $Pr_{0.5}(Ca,Sr)_{0.5}MnO_3$ series (23), which exhibits the same Mn^{+3}/Mn^{+4} ratio. This Ho compound has a $\langle r_A \rangle$ value close to that of $Pr_{0.5}Ca_{0.4}Sr_{0.1}MnO_3$ ($\langle r_A \rangle = 1.193$ Å) but a higher mismatch value ($\sigma^2 = 0.014$ Å^2 versus 0.0015 Å^2). At room temperature, both samples exhibit a *Pnma*-type

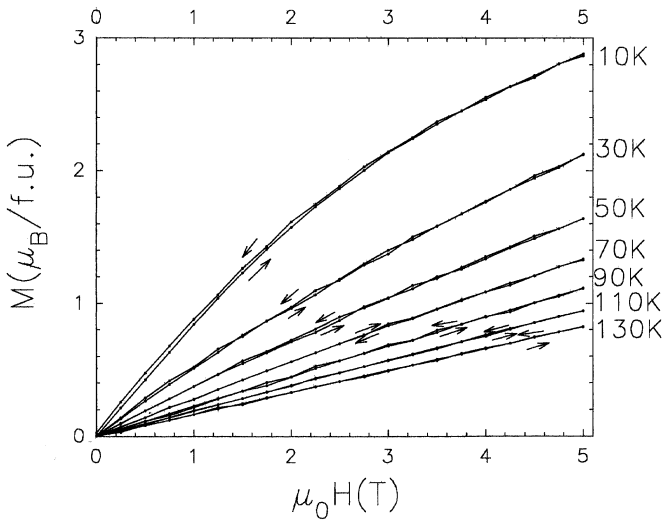

FIG. 12. Magnetic field dependence of the isothermal magnetization. T values are labeled on the graph.

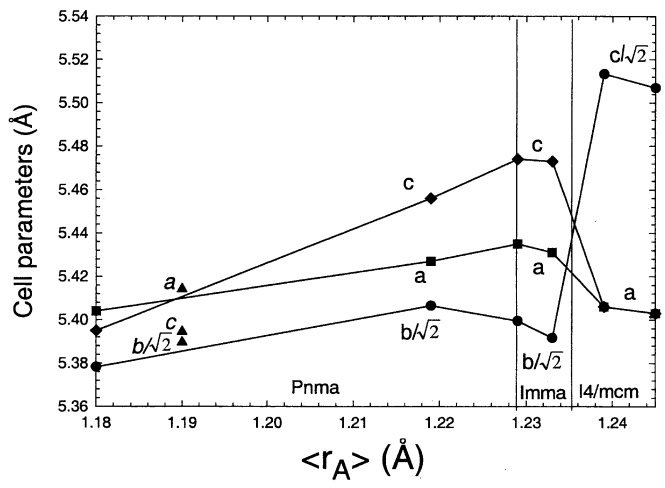

FIG. 14. $\langle r_A \rangle$ dependence of the cell parameters observed at room temperature in the $Pr_{0.5}(Sr,Ca)_{0.5}MnO_3$ series (from Ref. (23)). The triangles are for the Ho-based compound.

structure linked to the small $\langle r_A \rangle$ value, and the cell parameters, refined from 3T2 data for both series, are reported in Fig. 14. The structure is from O′ type for $Pr_{0.5}Ca_{0.4}Sr_{0.1}MnO_3$ and $Ho_{0.5}Sr_{0.5}MnO_3$ but the *a* and *c* cell parameters are more different for the Ho-based perovskite. At low temperature, both samples behave differently, $Pr_{0.5}Ca_{0.4}Sr_{0.1}MnO_3$ exhibits an AFM CE-type charge ordered structure, in contrast to the holmium perovskite, which exhibits a short-range *A*-type AFM state. It should be recalled that the CE-type AFM structure is associated with the 90° ordering of the Mn^{+3} d_z^2 orbitals, which is responsible for the stripes observed by electron microscopy, and that in this AFM structure the electrons are completely localized, unlike in the A-type AFM state. The lack of such ordering for $Ho_{0.5}Sr_{0.5}MnO_3$, exhibiting the same average *A*-site cationic size as $Pr_{0.5}Ca_{0.4}Sr_{0.1}MnO_3$, shows that a too high *A*-site cationic size mismatch hinders the establishment of the long-range orbital ordering. There is thus no doubt that the *A*-site mismatch is at the origin of the complex structure and microstructure of this perovskite and of its strained character.

REFERENCES

1. P. M. Woodward, D. E. Cox, T. Vogt, C. N. R. Rao, and A. K. Cheetham, *Chem. Mater.* **11,** 3528 (1999).
2. C. H. Chen and S. W. Cheong, *Phys. Rev. Lett.* **76,** 4042 (1996).
3. P. Radaelli, D. E. Cox, M. Marezio, and S. W. Cheong, *Phys. Rev. B* **55,** 3015 (1997).
4. Z. Jirak, S. Krupicka, Z. Simsa, M. Dlouha, and S. Vratislav, *J. Magn. Magn. Mater.* **53,** 153 (1985).
5. M. Hervieu, A. Barnabé, C. Martin, A. Maignan, F. Damay, and B. Raveau, *Eur. Phys. J. B.* **8,** 31 (1999).
6. A. Barnabé, M. Hervieu, C. Martin, A. Maignan, and B. Raveau, *J. Mater. Chem.* **8,** 1405 (1998).
7. F. Damay, Z. Jirak, M. Hervieu, C. Martin, A. Maignan, B. Raveau, G. André, and F. Bourée, *J. Magn. Magn. Mater.* **190,** 221 (1998).
8. E. O. Wollan, and W. C. Koehler, *Phys. Rev.* **100,** 545 (1955).
9. J. B. Goodenough, *Phys. Rev.* **100,** 564 (1955).
10. H. W. Kawano, R. Kujimoto, H. Yoshizawa, Y. Tomioka, H. Kuwahara, and Y. Tokura, *Phys. Rev. Lett.* **78,** 4253 (1997).
11. F. Damay, C. Martin, M. Hervieu, A.Maignan, B. Raveau, G. André, and F. Bourée, *J. Magn. Magn. Mater.* **184,** 71 (1998).
12. Y. Tomioka, A. Asamitsu, Y. Moritomo, H. Kuwahara, and Y.Tokura, *Phys. Rev. Lett.* **74,** 5108 (1995).
13. H. Kawana, R. Kajimoto, H. Yoshizawa, Y. Tomioka, H. Kuwahara, and Y. Tokura, *Phys. Rev. B* **78,** 4253 (1997).
14. P. M. Woodward, T. Vogt, D. E. Cox, A. Arulraj, C. N. R. Rao, P. Karen, and A. K. Cheetham, *Chem. Mater.* **10,** 3652 (1998).
15. B. Garcia-Landa, J. M. De Teresa, M. R. Ibarra, C. Ritter, R. Drost, and M. R. Lees, *J. Appl. Phys.* **83,** 7664 (1998).
16. T. Terai, T. Sasaki, T. Kakeshita, T. Fukuda, T. Saburi, H. Kitagawa, K. Kindo, and M. Honda, *Phys. Rev. B* 61, 3488 (2000).
17. M. Hervieu, G. Van Tendeloo, V. Caignaert, A. Maignan, and B. Raveau, *Phys. Rev. B* **53,** 14,274 (1996).
18. L. M. Rodriguez-Martinez, and J. P. Attfield, *Phys. Rev. B* **54,** 15,622 (1996).
19. E. Pollert, S. Krupicka, and E. Kuzmicova, *J. Phys. Chem. Solids* **43,** 1137 (1982).
20. A. M. Glazer, *Acta Crystallogr. Sect. B* **28,** 3385 (1972).
21. H. L. Yakel, W. C. Koehler, E. F. Bertaut, and F. Forrat, *Acta Crystallogr. Danem.* **16,** 957 (1963).
22. J. P. Attfield, *Chem. Mater.* **10,** 3239 (1998).
23. F. Damay, C. Martin, A. Maignan, M. Hervieu, B. Raveau, Z. Jirak, G. André, and F. Bourée, *Chem. Mater.* **11,** 536 (1999).